Journal of Materials Chemistry A

ROYAL SOCIETY OF CHEMISTRY

PAPER

View Article Online
View Journal | View Issue

Cite this: J. Mater. Chem. A, 2023, 11, 10319

Molecular interaction modulating Ruddlesden–Popper tin-based perovskite crystallization†

Han Pan,*[a] Yong Zheng,[a] Wenqing He,[a] Wenxing Yang,*[a] Xiu Gong,[b] Xiaodong Liu,[c] Qiang Wei,[d] Yan Liu,[e] Yan Shen[f] and Mingkui Wang*[f]

Received 14th February 2023
Accepted 16th April 2023

DOI: 10.1039/d3ta00873h

rsc.li/materials-a

Ruddlesden–Popper (RP) tin-based halide perovskites have attracted intensive attention because of unique properties such as low-toxicity and low-cost processability. However, the uncontrollable crystallization of RP tin-based perovskites from solvents leads to less perfect crystal orientation and thus poor absorber layers with pinholes. Here, we propose an effective method to slow down crystallization kinetics *via* regulating the competition between intra- and intermolecular interactions in RP tin-based perovskites. Introducing an electron-rich heterocyclic thiophene rather than the traditional benzene ring into bulky spacers (*i.e.*, 2-thiophenemethylammonium cation, abbreviated as TH^+) can decrease the intermolecular interaction between iodostannic sheets and spacer cations but increase intramolecular interactions in spacer cations. A weak intermolecular interaction increases the strength of electrostatic repulsion between charged colloids, and thus stabilizes colloids. Such stable colloids could retard sol–gel transition before crystal formation, offering a wider processing window for orderly crystal growth of RP tin-based perovskites. The interlayer heterocyclic spacer interaction induces a subsequently ordered self-assembly of gels to reduce morphological defects. The $TH_2FA_3Sn_4I_{13}$ perovskite solar cell exhibits a two-fold improvement in power conversion efficiency compared to the control sample.

Introduction

Recently, the eco-friendly two-dimensional (2D) Ruddlesden–Popper (RP) tin halide perovskites have attracted considerable attention for solar cell application owing to improved moisture resistance capability and unique optical properties compared to their three dimensional counterparts.[1,2] RP tin iodide perovskites have the general chemical formula $R_2A_{n-1}Sn_nI_{3n+1}$, where R represents a bulky organic ammonium cation, A is $CH_3NH_3^+$ or $HC(NH_2)_2^+$ (FA^+), and n is an integer.[3] As the choice of bulky organic ammonium cations for RP tin-based perovskites is not limited by Goldschmidt's concept of ionic tolerance factors, it offers more flexibility and tunability in regulating the structure and band gaps from 1.83 eV ($n = 1$) to 1.43 eV ($n = 4$). These features perfectly fit the requirements for absorbing materials in tandem solar cells no matter whether employed in the top or bottom sub-cells.[4,5] A fast reaction between iodostannic compounds such as SnI_2 (high Lewis acidity) and organic ammonium salts such as FAI (Lewis bases) increases the crystallization speed of tin-based perovskites during the sol–gel film formation.[6,7] Therefore, this quick crystallization leaves the diffusion and reconstruction of clusters behind toward the uniform and ordered RP perovskite phase compounds. The competition of crystallization and reconstruction kinetics leads to poor-quality thin films with visible pinholes and disordered crystal orientation, and to final low-efficiency photovoltaic devices.[8,9] Currently, the highest reported photovoltaic efficiency based on 2D RP tin halide perovskite ($n = 4$) is 10.36%,[10] far lower than its Shockley–Queisser limit value (~32%).[11]

Several efforts have been made to control the crystallization process of RP tin-based perovskites *via* additives,[12–14] solvents,[15,16] and composition engineering.[17,18] For example, poly(4-vinylphenol) and poly(vinyl pyrrolidone) were employed to increase nucleation sites, improving the morphology and crystallization of RP tin-based perovskite films.[12] Li *et al.* introduced high-boiling point ionic liquid solvent *n*-butylammonium acetate (BAAc) into RP tin-based perovskites.[15] Through the coordination between BAAc and SnI_2, the formation of intermediates in the crystallization process could result in a high-quality film. The widely-used iodide anion for the RP tin perovskite precursor has

[a]School of Physics and Optoelectronic Engineering, Yangtze University, Jingzhou 434023, P. R. China. E-mail: hanpanph@163.com; wenxingyang2@126.com
[b]College of Physics, Guizhou Province Key Laboratory for Photoelectrics Technology and Application, Guizhou University, Guiyang 550025, P. R. China
[c]College of Chemistry and Environmental Engineering, Yangtze University, Jingzhou 434023, P. R. China
[d]State Key Laboratory of Heavy Oil Processing, China University of Petroleum, Beijing 102249, China
[e]School of Physics and Optoelectronic Engineering, Ludong University, Yantai, 264025, China
[f]Wuhan National Laboratory for Optoelectronics, School of Optoelectronic Science and Engineering, Huazhong University of Science and Technology, Wuhan 430074, P. R. China. E-mail: mingkui.wang@mail.hust.edu.cn

† Electronic supplementary information (ESI) available. See DOI: https://doi.org/10.1039/d3ta00873h

been partly replaced with acetate and tetrafluoroborate anions to coordinate with SnI_2 and bulky organic ammonium cations in precursors.[18] This method delays the speed of crystallization and thus induces highly oriented growth of RP tin perovskites. These reports unveil the critical role of precursor solution chemistry in perovskite crystallization, despite the inevitable presence of residual impurities in films due to the introduction of non-raw materials for resulting perovskites.

So far, perovskite precursors have been widely considered as colloidal dispersions in solution whose sizes are in the range from nanometers to sub-micrometers.[19,20] Therefore, these colloids composed of tin polyhalide frameworks formed from organic and inorganic components primarily determine the quality of deposited thin films and thus offer opportunities to structurally tune the coordination degree.[21,22] For example, the crystallization kinetics of $FASnI_3$ can be modulated by introduction of pre-nucleation clusters to decrease nucleation energy barriers, thus resulting in perovskite films of high-quality.[23] Despite progress in controlling crystallization of perovskites through facial colloidal engineering, the process from colloidal sol-to-gel to ultimate RP tin-based perovskite films to date provides only limited understanding for the control of morphological and structural properties. Indeed, stable colloids could delay the gelation, which determines the crystallization of thin films.[24,25] According to the Stern–Gouy–Chapman (SGC) theory, an electrostatic repulsive force increases with colloidal charges, leading to more stable colloids. In this consideration, bulky organic ammonium cations could be developed to decrease the attraction between those cations and iodostannic components for increasing the negative charges on the surface of colloids.

This study proposes a novel strategy to improve the crystallization of RP tin-based perovskites by weakening intermolecular interaction between iodostannic sheets and spacer cations through strengthening intramolecular interactions in spacer cations. We explored the possibility of using two ammonium derivatives differing only in the polar moiety, *i.e.*, 2-thiophenemethylammonium cation (TH^+) and benzylamine cation (BE^+) as spacers. Instead of the conventional benzene ring, the electron-rich heterocycle, such as thiophene for example, can enhance the interaction between that and the electron-deficient ammonium group in spacer cations, thus decreasing the intermolecular interaction between iodostannic and ammonium components. The competing intramolecular and intermolecular interactions could stabilize the colloidal perovskite nanoparticles, which retards the gelation process and promotes the oriented crystal growth of RP tin-based perovskites. The π–H interactions among adjacent cations facilitate the formation of pinhole-free perovskite films. Consequently, the $TH_2FA_3Sn_4I_{13}$ perovskite solar cell with a structure of ITO/PEDOT:PSS/perovskite/PCBM/BCP/Ag achieved a high PCE of 9.03%, which is among the highest efficiency of the reported state-of-the-art 2D RP tin perovskite solar cells.

Results and discussion

This study focuses on the effect of competition between intramolecular and intermolecular interactions on the RP perovskite

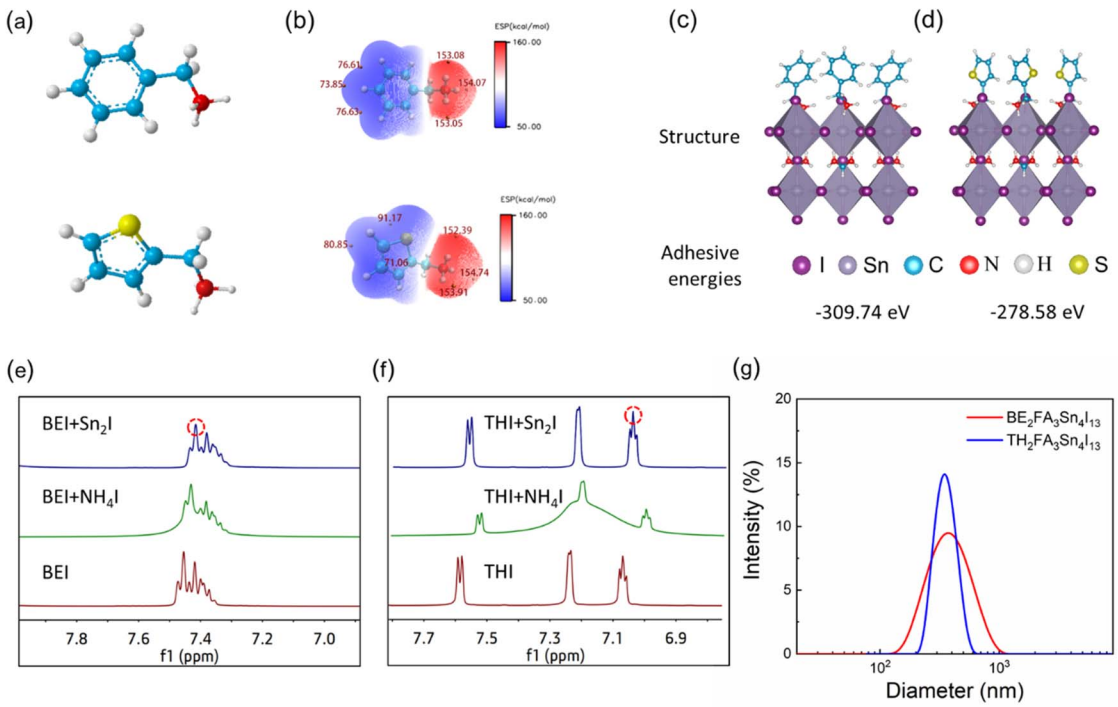

Fig. 1 (a) Chemical structures of BE^+ (up) and TH^+ (down) spacers. (b) The electrostatic potential surface distributions of BE^+ (up) and TH^+ (down). Optimized geometrical structures and adhesive energies of (c) $BE_2FA_3Sn_4I_{13}$-based and (d) $TH_2FA_3Sn_4I_{13}$-based samples. ^1H NMR signals measured for (e) BEI, compounds of BEI and NH4I, and compounds of BEI and SnI_2, and (f) THI, compounds of THI and NH_4I, and compounds of THI and SnI_2 in deuterated DMSO solution. (g) The colloid size distributions in the precursor solutions prepared with BEI and THI.

sol-to-gel transition process. This transition occurs during the spin-coating stage followed by subsequent thermal decomposition of the gel to form perovskite films during the annealing process.[26,27] The proof of concept is implemented with RP tin perovskite ($R_2FA_3Sn_4I_{13}$) thin-film fabrication, in which a benzylamine cation (BE^+, Fig. 1a, up), and a 2-thiophenemethylammonium cation (TH^+, Fig. 1a, down) are used as spacers. These two chemicals have a basic molecular structure in common, *i.e.*, an electron-deficient ammonium unit, and only a difference in the end group, *i.e.*, a benzyl for BEI and a thiophene for THI. The latter probably brings up a strong intramolecular electron push–pull effect due to the electron-rich properties of thiophene.

The electrostatic potential surface (EPS) distributions of BE^+ and TH^+ cation models were evaluated with density functional theory (DFT) calculations and the results are mapped in Fig. 1b. The difference between the maximal and minimal values of the ESP for the TH^+ cation (154.74 and 80.58 kcal mol^{-1}, respectively) is larger than that of the BE^+ cation (154.07 and 73.84 kcal mol^{-1}, respectively). This indicates that the intramolecular interaction in the TH^+ cation is stronger than that in the BE^+ cation. DFT calculations on the adhesive energy were carried out to figure out the interaction between spacer cations and tin iodide. The energy of TH^+ adhered to the inorganic sheet surface was calculated to be −278.58 eV, higher than that of BE^+ (−309.74 eV), indicating negatively charged inorganic sheets are easily inclined to attract BE^+ cations (Fig. 1c, d and S1†).

We quantified the component interaction in the precursor solution using ^1H nuclear magnetic resonance (NMR) spectroscopy measurements. Herein, NH_4I was used to offer NH_4^+ to simulate the center of the positive charge in spacer cations. As shown in Fig. 1e and f, the chemical shift (δ) for the proton signal from the benzene ring (the peak marked with red dotted lines for example) moves from 7.45 ppm to 7.43 ppm, and that from the thiophene group shifts to 7.07 ppm from 7.00 ppm when adding NH_4I into the deuterated solution containing the spacer cations. A larger change of δ in this case indicates stronger intramolecular interaction between electron-rich heterocyclic thiophene and the electron-deficient ammonium group in the TH^+ cation. In turn, when SnI_2 was added, the ^1H resonance at 7.42 ppm was detected for the benzene ring and at 7.06 ppm for that of the thiophene group. A slight shift of δ implies the weak interaction between TH^+ and tin iodide compounds. It's appropriate to infer that the electron-rich heterocycle could enhance the intramolecular interaction in spacer cations, but weaken the intermolecular interaction between spacer cations and tin iodide components.

We further conducted X-ray photoelectron spectroscopy (XPS) measurements on the RP tin-based perovskite films to investigate molecular interaction. The binding energy for N 1s of BEI and $BE_2FA_3Sn_4I_{13}$ was found to be 400.1 and 401.7 eV, and 400.1 and 401.4 eV for THI and $TH_2FA_3Sn_4I_{13}$ (Fig. S2a†), respectively. A smaller shift of binding energy between ammonium salt and perovskite (*i.e.*, 1.3 eV for THI and $TH_2FA_3Sn_4I_{13}$ in this study) indicates a weak interaction between the spacer cation and the tin iodide compounds. Fig. S2b† shows the Fourier transform infrared (FT-IR) spectra of ammonium salts and corresponding RP perovskites. In comparison with a large shift of the NH_3^+ stretching vibration peak from 3002 cm^{-1} (BEI) to 2969 cm^{-1} ($BE_2FA_3Sn_4I_{13}$), the smaller change from 2983 cm^{-1} (THI) to 2972 cm^{-1} ($TH_2FA_3Sn_4I_{13}$) also suggests a weak interaction between TH^+ and iodostannic compounds.

The dynamic light scattering (DLS) technique was used to investigate the effect of electron-rich groups on the colloid size in perovskite precursor solution. Fig. 1g shows the particle size distribution counted in percentage of different precursor solutions. The particle diameter of colloids in $BE_2FA_3Sn_4I_{13}$ perovskite precursor solution shows a wide distribution from 140 nm to 955 nm centred at ~342 nm. However in the $TH_2FA_3Sn_4I_{13}$ perovskite precursor solution, the colloids exhibit narrow particle size distribution centred at ~365 nm. Uniform colloidal clusters are beneficial for self-assembling into high-quality films.[28–30]

The zeta potential of particles is a key indicator of the stability of a colloidal dispersion, like nanoparticles or liposomes, since it reflects the ability of particles to repulse each other electrostatically.[31] The higher the absolute value of zeta potential, the greater the stability of the colloidal system. As shown in Fig. 2a, the absolute value of zeta potential increases from 0.426 to 0.897 mV by switching the spacer component from BEI to THI, indicating that the colloidal system based on THI possesses a higher stability. The higher zeta potential of the TH^+-based sample could be attributed to the increased colloidal charges, which can be associated with the electron-rich moiety dependent molecular interaction as discussed below.

The subsequent colloid gelation is a process of aggregation and fusion growth of colloids. The aggregation kinetics of colloidal systems were further investigated with time-resolved DLS techniques.[32,33] Fig. 2b presents the intensity-weighted hydrodynamic diameter (D_h) of colloid solutions continuously recorded for every 30 s over 30 min. The attachment efficiency (α) is introduced to describe the relationship between the aggregation and perovskite precursor concentration, which can be calculated by normalizing the measured k value with the aggregation rate constant in the diffusion-limited aggregation (DLA) regime (k_{fast}) according to the following equation.[34]

$$\alpha = \frac{k}{k_{fast}} = \frac{\left(\frac{dD_h(t)}{dt}\right)_{t\to 0}}{\left(\frac{dD_h(t)}{dt}\right)_{t\to 0,\ fast}} \quad (1)$$

where the subscript 'fast' represents DLA conditions, and k is the initial aggregation rate constant of colloids, which can be determined by the initial increase of the hydrodynamic diameter D_h with time t in the period from aggregation initiation (t_0) to the time when D_h reached 1.25 (ESI, S3a and b†).[30] As shown in Fig. 2b, the attachment efficiency (α) values of both samples increased with perovskite precursor concentration till a stable α value ($\alpha = 1$). The value of α less than 1 indicates a slow, reaction-limited cluster aggregation (RLA) dominated by interparticle interaction with an energy barrier.[29] Compared to the $BE_2FA_3Sn_4I_{13}$-based colloid (0.25 at 0.1 mol), the $TH_2FA_3Sn_4I_{13}$-based colloid has a lower α (0.12 at 0.1 mol) in the RLA regime at

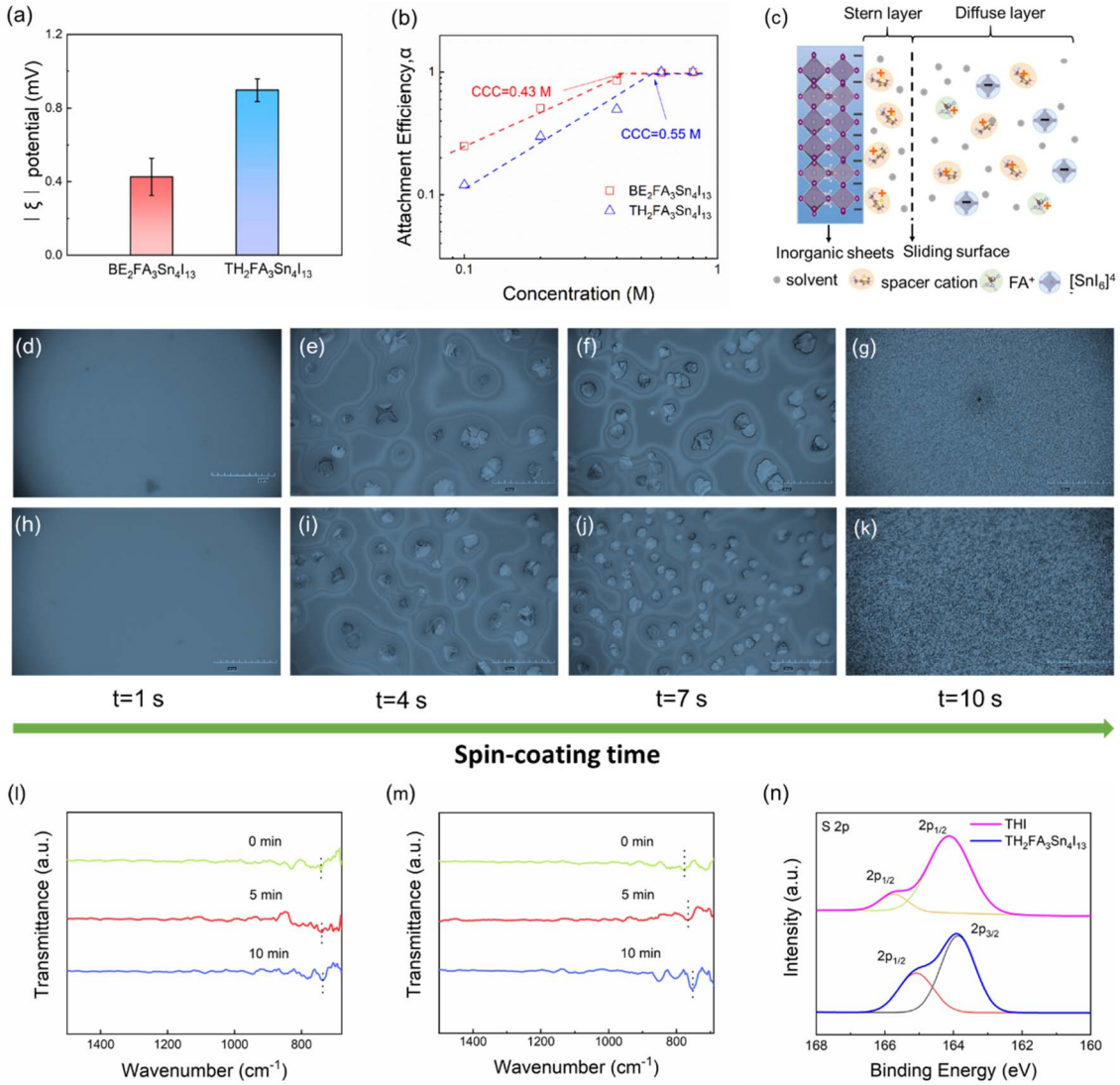

Fig. 2 (a) The absolute zeta potential of $BE_2FA_3Sn_4I_{13}$ and $TH_2FA_3Sn_4I_{13}$ in the perovskite precursor solutions. The error bars are mean ± standard deviation from measurements of 10 different samples. (b) The attachment efficiency of $BE_2FA_3Sn_4I_{13}$-based and $TH_2FA_3Sn_4I_{13}$-based colloids as a function of perovskite precursor concentration. (c) Schematic illustration of the double layer mode. Optical characterization of the growth process of (d to g) $BE_2FA_3Sn_4I_{13}$-based perovskite and of (h to k) $TH_2FA_3Sn_4I_{13}$-based perovskite as a function of spin-coating time. FT-IR spectroscopy characterization of (l) $BE_2FA_3Sn_4I_{13}$-based and (m) $TH_2FA_3Sn_4I_{13}$-based samples during thermal annealing for 0 min, 5 min and 10 min. Dotted lines represent the out-of-plane bending vibration of C–H. (n) X-ray photoelectron spectra of S 2p for THI and $TH_2FA_3Sn_4I_{13}$.

any given concentration, which could result from the stronger repulsion between $TH_2FA_3Sn_4I_{13}$-based colloids.

This was further verified by measuring their critical coagulation concentrations (CCCs) by extrapolating the linear plots of logarithmic of α values *versus* concentrations in RLA and DLA regimes. As illustrated in Fig. 2b, the CCC values are about ~0.43 and ~0.55 mol for $BE_2FA_3Sn_4I_{13}$-based and $TH_2FA_3Sn_4I_{13}$-based colloids, respectively. This indicates that $TH_2FA_3Sn_4I_{13}$-based colloids need a higher concentration to cause rapid coagulation. In short, the $TH_2FA_3Sn_4I_{13}$-based cation could delay colloid gelation to form orderly self-assembly of perovskite segments, which is helpful to an oriented growth of perovskite crystals, and thus improves the film quality.

Fig. 2c illustrates the attraction of spacer cations, as the counterion layer, to the inorganic sheets based on the SGC model of the double layer theory.[35] Generally, the inorganic iodostannic components could be regarded as colloidal cores and the organic components as Stern and diffusion layers. As a weak interaction leads to less TH^+ entering the interior of the slip plane, the electric quantity of colloidal particles increases as well as zeta potential raises. Compared to the BE^+-based colloids, the TH^+-based colloids have a stronger electrostatic repulsion to hinder particle aggregation, which could delay the sol–gel transition and slow down the crystallization rate. We performed optical microscopy characterization to visualize the process from sol to gel during the spin-coating process. The details are given in the ESI.† Fig. 2d–g show, for the case of the $BE_2FA_3Sn_4I_{13}$-based perovskite, the formation of particles with non-uniform sizes on the substrate surface. Some aggregated particles together appear after spin-coating for 1 s. These

aggregates with different sizes and shapes further form agglomerates as the deposition goes on (Fig. 2e and f). After dripping chlorobenzene, the three-dimensional network structure of gelatine forms. The $BE_2FA_3Sn_4I_{13}$-based gelatin film shows the morphology of irregularity and voids (Fig. 2g). For the case of the $TH_2FA_3Sn_4I_{13}$-based perovskite, the particles remain stable in the beginning (Fig. 2h). Then colloids self-assembled into structured aggregates with a similar size and shape (Fig. 2i and j), triggering a uniform and continuous gelatin film (Fig. 2k).

Gelatin films were further annealed at 100 °C for 10 minutes to drive off the residual solvents. We performed FT-IR measurements on these films during this annealing procedure. As shown in Fig. 2l, the out-of-plane bending vibration peak of C–H at 740 cm^{-1} in the $BE_2FA_3Sn_4I_{13}$-based sample does not significantly change before and after the annealing whereas in Fig. 2m that at 776 cm^{-1} in the $TH_2FA_3Sn_4I_{13}$-based sample shifts to a lower wavenumber at 765 (5 min) and 753 cm^{-1} (10 min). The larger shift probably results from π···H hydrogen bonds in the adjacent thiophene group in $TH_2FA_3Sn_4I_{13}$-based samples. We further used XPS to identify the interlayer interaction. The characteristic peaks of S 2p at 164.1 and 165.7 eV for THI shift to lower binding energies of 163.8 and 165.1 eV for $TH_2FA_3Sn_4I_{13}$ (Fig. 2n). In contrast, no shifts in the C (1s), N (1s), Sn (3d) and I (3d) were detected when we compared the XPS spectra of $TH_2FA_3Sn_4I_{13}$ and three-dimensional $FASnI_3$ (Fig. S4†). We deduce negligible interactions occur between S and other elements, such as C, N, Sn and I. However, a shift in S 2p probably results from the interactions among adjacent spacer cations.[36] Such an interlayer interaction may induce gel self-assembly in favour of the formation of a high-quality film.

Fig. 3a and b show the top-view scanning electron microscopy (SEM) images of the control $BE_2FA_3Sn_4I_{13}$ and $TH_2FA_3Sn_4I_{13}$ perovskite films, respectively. We observed that the films of $TH_2FA_3Sn_4I_{13}$ are more compact, more uniform and less pinhole-free compared to the film of $BE_2FA_3Sn_4I_{13}$. Fig. S5† shows the X-ray diffraction (XRD) patterns of both perovskite films. The similar diffraction peaks at ~14.0° and ~28.2° correspond to the (111) and (202) planes, respectively.[20,37] The lack of (0k0) peaks in the $TH_2FA_3Sn_4I_{13}$-based film suggests the vertical growth of the perovskite compounds, which could facilitate efficient charge transport. The grazing-incidence wide-angle X-ray scattering (GIWAXS) measurements were performed to explore the crystal structure in perovskite films. The observation of Debye–Scherrer rings in the $BE_2FA_3Sn_4I_{13}$-based films indicates an almost random orientation of the crystal grains (Fig. 3c). By contrast, in the $TH_2FA_3Sn_4I_{13}$-based film (Fig. 3d), sharp and discrete Bragg spots of (111) and (202) diffractions are observed, indicating high crystallization and a preferred orientation parallel to the substrate surface.[17,21] This can be due to slower crystallization of $TH_2FA_3Sn_4I_{13}$-based perovskite, which accesses a much wider processing window for diffusion and reconstruction of clusters and orderly crystal growth. Given the nonconductive nature of the bulky organic cations in layered RP perovskites, the perpendicular orientation growth of the $TH_2FA_3Sn_4I_{13}$-based sample facilitates carrier transport.

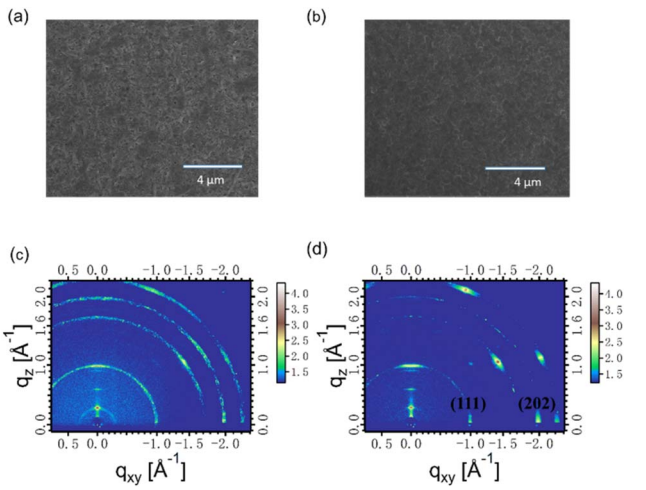

Fig. 3 The top-view SEM images and GIWAXS pattern of $(BE)_2FA_3Sn_4I_{13}$ (a, c) and (b) $(TH)_2FA_3Sn_4I_{13}$ films (b, d).

The carrier dynamics of RP tin-based perovskite films were investigated by photoluminescence (PL) spectroscopy. Notably, the steady-state PL peak intensity of the $TH_2FA_3Sn_4I_{13}$-based film is increased to about two times relative to that of the $BE_2FA_3Sn_4I_{13}$-based film (Fig. S6†). Time-resolved photoluminescence (TRPL) curves of RP perovskite films were fitted using a bi-exponential decay equation, in which the fast decay component (τ_1) is assigned to the surface recombination and the slow decay component (τ_2) is associated with the bulk component recombination (Fig. 4a).[38,39] The τ_1 and τ_2 were 5.88 and 26.35 ns for the $BE_2FA_3Sn_4I_{13}$-based film, respectively. In comparison, both τ_1 and τ_2 increased to 9.36 and 38.81 ns for the $TH_2FA_3Sn_4I_{13}$-based film, indicating a lower defect density.[40,41]

To further verify the reduction of the trap density in the $TH_2FA_3Sn_4I_{13}$-based film, we fabricated the electron-only and hole-only devices with the configuration of ITO/SnO_2/perovskite/PCBM/BCP/Ag and ITO/PEDOT:PSS/perovskite/Spiro-OMeTAD/Au, respectively (Fig. 4b and c). The electron and hole trap densities for the $TH_2FA_3Sn_4I_{13}$-based film were 3.26 × 10^{16} and 3.74 × 10^{16} cm^{-3}, respectively, which is lower than those for the $BE_2FA_3Sn_4I_{13}$-based film (7.65 × 10^{16} and 8.14 × 10^{16} cm^{-3}, respectively). The decreasing defect density could be attributed to the controlled crystal growth. We also calculated the mobility (μ) of the RP perovskite film according to the Mott–Gurney law:[41]

$$J = \frac{8}{9}\mu\varepsilon_0\varepsilon_r\frac{V^2}{L^3} \quad (2)$$

where V is the base voltage and J is the current density. The electron and hole mobility of the $TH_2FA_3Sn_4I_{13}$-based film were estimated to be 8.21 × 10^{-3} and 6.72 × 10^{-3} cm^2 V^{-1} s^{-1}, respectively, higher than those of the control film (7.57 × 10^{-4} and 2.95 × 10^{-4} cm^2 V^{-1} s^{-1}, respectively). The improved carrier mobility of $TH_2FA_3Sn_4I_{13}$ could be attributed to the vertical orientation of inorganic components which facilitates carrier transport and the π–π interaction in adjacent cations which enhances carrier transport across spacer molecules.[42–44]

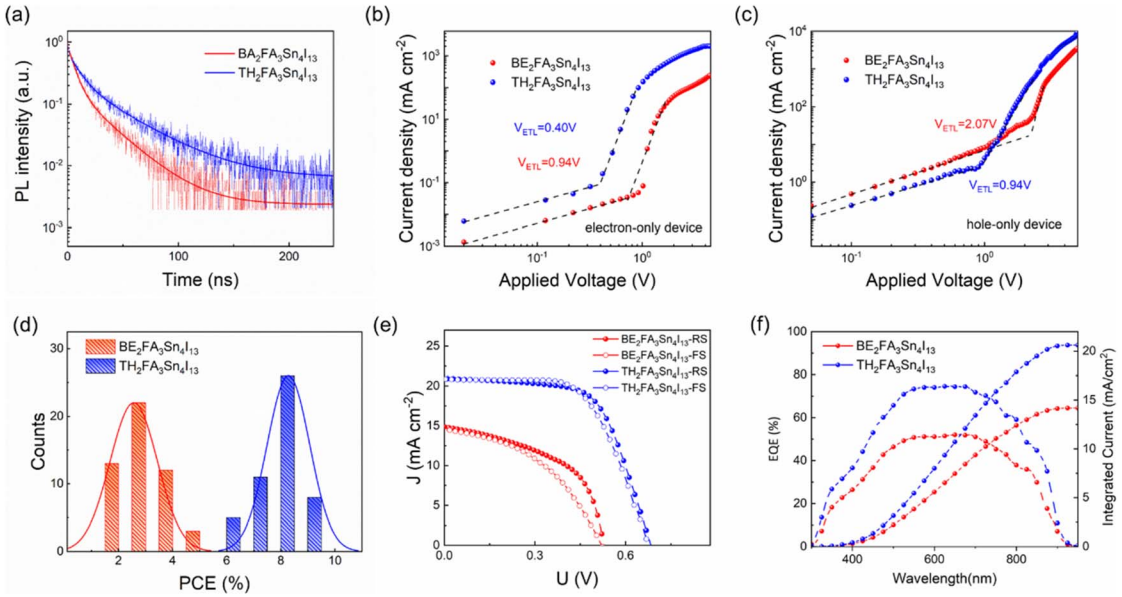

Fig. 4 (a) The TRPL curves of the $BE_2FA_3Sn_4I_{13}$-based and $TH_2FA_3Sn_4I_{13}$-based perovskite films on the glass substrate. Dark *J*–*V* measurements of (b) electron- and (c) hole-only devices based on the $BE_2FA_3Sn_4I_{13}$-based and $TH_2FA_3Sn_4I_{13}$-based perovskites. (d) The PCE histogram of 50 devices based on $BE_2FA_3Sn_4I_{13}$ and $TH_2FA_3Sn_4I_{13}$ perovskites. (e) Photocurrent *J*–*V* curves in reverse scan (RS) and forward scan (FS) directions of and (f) The EQE spectra and integrated current of the champion devices based on $BE_2FA_3Sn_4I_{13}$ and $TH_2FA_3Sn_4I_{13}$ perovskites.

Photovoltaic performances of the $TH_2FA_3Sn_4I_{13}$-based PSCs were evaluated using the planar architecture of ITO/PEDOT:PSS/perovskite/PCBM/BCP/Ag. The photovoltaic performances of devices were measured under standard AM 1.5 G (100 mW cm^{-2}) illumination. Both of the $BE_2FA_3Sn_4I_{13}$-based and $TH_2FA_3Sn_4I_{13}$-based devices exhibit great reproducibility with an average PCE of 2.59% and 8.26%, respectively (Fig. 4d). Fig. 4e shows the photocurrent density–voltage (*J*–*V*) curves of the best-performing RP PSCs, and the corresponding photovoltaic parameters are summarized in Table S1.† The control device exhibits a PCE of only 4.04% with a V_{oc} of 0.53 V, a J_{sc} of 14.88 mA cm^{-2} and a fill factor (FF) of 51.2%. Meanwhile, the PCE of the $TH_2FA_3Sn_4I_{13}$-based device increases to 9.03%, with a V_{oc} of 0.68 V, a J_{sc} of 20.94 mA cm^{-2} and an FF of 63.4%. The enhancement in PCE is attributed to the V_{oc} and J_{sc}. Compared to the $BA_2FA_3Sn_4I_{13}$-based device, the $TH_2FA_3Sn_4I_{13}$-based device exhibits a negligible photocurrent hysteresis, as indicated by the similar *J*–*V* curves in different scan directions, which could be attributed to the reduced defects (Fig. 4e).[45,46] Fig. 4f illustrates the external quantum efficiency (EQE) spectra of both best-performing devices. The integrated photocurrent densities of the $BA_2FA_3Sn_4I_{13}$-based and $TH_2FA_3Sn_4I_{13}$-based devices calculated from the EQE spectrum are 14.21 and 20.65 mA cm^{-2}, respectively, in good agreement with the measured J_{sc} from the *J*–*V* curves.

We further fitted the semi-log plot of EQE values *versus* photon energy to investigate band tails of RP tin-based perovskites. Estimated from the first EQE derivative, the bandgaps of $BE_2FA_3Sn_4I_{13}$-based and $TH_2FA_3Sn_4I_{13}$-based perovskites are both 1.33 eV (Fig. S7†), indicating similar structures. Moreover, the Urbach energy (E_u) of the absorbers was calculated from the exponential absorption tail in the long-wavelength edge of their EQE according to the equation.[47]

$$\mathrm{EQE} = \mathrm{EQE}_0 \exp[(E - E_g)/E_u] \quad (3)$$

where EQE_0 is the EQE value at the bandgap (E_g). The E_u of the $TH_2FA_3Sn_4I_{13}$-based film is 22.4 meV, obviously lower than that of the $BE_2FA_3Sn_4I_{13}$-based film (28.7 meV), suggesting a low structural disorder and low density of traps in the $TH_2FA_3Sn_4I_{13}$-based film. Such a well-ordered microstructure of $TH_2FA_3Sn_4I_{13}$-based perovskites could suppress charge carrier recombination and facilitate carrier transportation, enhancing the device's V_{oc}.

Transient photocurrent/photovoltage (TPC/TPV) decay measurements were performed to characterize the carrier transportation and recombination in the RP tin-based perovskite devices under illumination of various intensities (Fig. S8†). Fig. 5a and b show the carrier recombination lifetimes (τ_{re}) and transport lifetimes (τ_{tr}) for $BA_2FA_3Sn_4I_{13}$-based and $TH_2FA_3Sn_4I_{13}$-based devices, which were obtained by bi-exponential fitting of the TPV/TPC curves. Compared to the $BE_2FA_3Sn_4I_{13}$-based device, the $TH_2FA_3Sn_4I_{13}$-based device shows longer recombination lifetimes and shorter carrier transport lifetimes of both electron and hole carriers, indicating that the $TH_2FA_3Sn_4I_{13}$-based device has less defect traps and higher charge collection, which could demonstrate the increase of all the photovoltaic parameters, *i.e.*, J_{sc}, V_{oc}, and FF. The diffusion length (*L*) of devices could be further calculated based on the following equation.[48,49]

$$L = d\sqrt{\frac{\tau_{rec}}{c\tau_{tr}}} \quad (4)$$

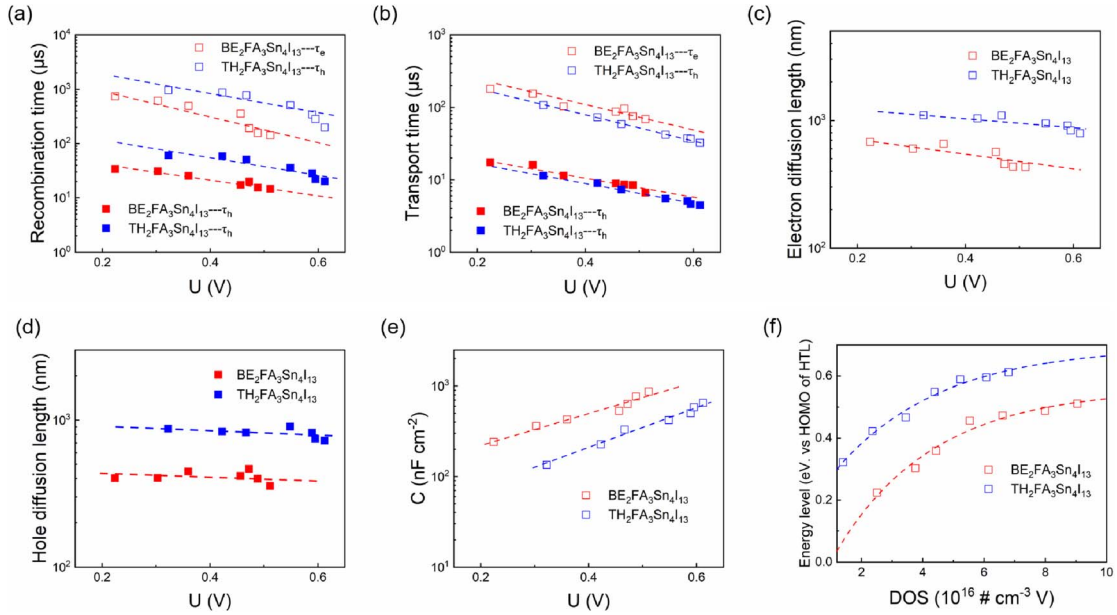

Fig. 5 (a) Charge recombination time, (b) transport time, (c) calculated electron diffusion length, (d) hole diffusion length, (e) capacitance, and (f) corresponding density of states (DOS) of the $BE_2FA_3Sn_4I_{13}$-based and $TH_2FA_3Sn_4I_{13}$-based devices.

where d is the film thickness, and c is a constant which is correlated with the charge conduction mechanism. Under one sun illumination, the electron and hole diffusion lengths are estimated to be 792 nm and 725 nm, respectively, for the $TH_2FA_3Sn_4I_{13}$-based device, being longer than that of 431 nm for electrons and 356 nm for holes in the $BA_2FA_3Sn_4I_{13}$-based device (Fig. 5c and d). A long diffusion length guarantees effective charge collection.

The capacitance at open circuit potential was further obtained by integrating a short-circuit photocurrent. Obviously, the $TH_2FA_3Sn_4I_{13}$-based device shows a smaller capacitance compared to the $BA_2FA_3Sn_4I_{13}$-based device as shown in Fig. 5e, indicating the retarded recombination of the trapped charge carriers in the former. Furthermore, we characterized the density of trap state distribution by extracting the capacitance (Fig. 5f).[50] The $TH_2FA_3Sn_4I_{13}$-based device has an apparent low density of trap states at a given energy level compared to the $BE_2FA_3Sn_4I_{13}$-based device, probably resulting from the high-quality film.

After air exposure (RH $\approx$ 20%) for 24 h, the unencapsulated $TH_2FA_3Sn_4I_{13}$-based device maintains more than 90% of their original efficiency, whereas that for the $BE_2FA_3Sn_4I_{13}$-based device decreases by 50% (in Fig. S9†). The better ambient stability of the $TH_2FA_3Sn_4I_{13}$-based device is mainly attributed to the reduced defect of the perovskite film which resists the hydrolyzation and oxidation.

The method of regulating molecular interaction to modulate crystallization can be extended to most of the RP tin-based perovskites. For instance, in order to verify its validity we have further prepared an $FU_2FA_3Sn_4I_{13}$ RP perovskite film using the 2-furfurylammonium cation (FU^+) composed of electron-rich furan as the spacer cation. The SEM image characterization shows a uniform pinhole-free surface (Fig. S10a†). The GIWAXS pattern of the $FU_2FA_3Sn_4I_{13}$ samples clearly exhibits the sharp and discrete Bragg spots of (111) and (202) diffractions, indicating a highly oriented growth of the RP phases with the inorganic components perpendicular to substrates (Fig. S10b†). The J–V curve of the best-performing $FU_2FA_3Sn_4I_{13}$-based perovskite is shown in Fig. S11.† The device exhibits a PCE of 8.62% with a V_{oc} of 0.67 V, a J_{sc} of 20.12 mA cm^{-2} and a FF of 63.9%. Therefore, we believe that the strategy could be capable of fabricating RP tin-based perovskite solar cells with high efficacy and stability.

Conclusions

In summary, we have demonstrated that electron-rich heterocycle controlled competing intramolecular and intermolecular interactions could effectively improve crystallization quality of RP tin-based perovskites by regulating colloid gelation and thermal decomposition of the gel. For the proof of concept, electron-rich thiophene as a substitute for the phenyl group in BE^+ is designed and synthesized for RP perovskite $TH_2FA_3Sn_4I_{13}$. We have shown that the increase in intramolecular interactions in spacer cations by such substituents could decrease the intermolecular interaction between iodostannic sheets and spacer cations. The method stabilizes colloids and retards sol–gel transition, facilitating the oriented crystal growth. Moreover, the π-H interactions among interlayer heterocyclic spacers induce ordered self-assembly of gels, leading to a high-quality film. Compared to the $BE_2FA_3Sn_4I_{13}$-based device, the $TH_2FA_3Sn_4I_{13}$-based device with the electron-rich thiophene group attained a higher PCE of 9.03% and air stability. This approach provides a facile method toward developing efficient and stable RP tin-based perovskites.

Author contributions

H. P. conducted the device fabrication and prepared the manuscript. H. P., Y. Z. and W. H. synthesized the materials and

measured the device performance. X. L., Q. W. and Y. L. performed the calculations. X. G., Y. S. and W. Y. revised the manuscript. M. W. guided and supervised the whole study. All authors contributed to the discussion.

Conflicts of interest

There are no conflicts to declare.

Acknowledgements

The authors acknowledge financial support from the National Natural Science Foundation of China (No. 12075036 and 21975088), Research Foundation of Yangtze University (No. 8021003102-2022), the Science Foundation of Educational Commission of Hubei Province of China (No. T2020008), and the Cultivation Programs Research Foundation of Guizhou University (No. 2019-64).

References

1 N. Zibouche and M. Islam, *ACS Appl. Mater. Interfaces*, 2020, **12**, 15328–15337.
2 T. Macdonald, L. Lanzetta, X. Liang, D. Ding and S. Haque, *Adv. Mater.*, 2022, 2206684.
3 M. P. Arciniegas and L. Manna, *ACS Energy Lett.*, 2022, **7**, 2944–2953.
4 T. Wu, D. Cui, X. Liu, X. Luo, H. Su, H. Segawa, Y. Zhang, Y. Wang and L. Han, *Sol. RRL*, 2021, **5**, 2100034.
5 F. Li, Y. Xie, Y. Hu, M. Long, Y. Zhang, J. Xu, M. Qin, X. Lu and M. Liu, *ACS Energy Lett.*, 2020, **5**, 1422–1429.
6 Q. Chen, J. Luo, R. He, H. Lai, S. Ren, Y. Jiang, Z. Wan, W. Wang, X. Hao and Y. Wang, *Adv. Energy Mater.*, 2021, **11**, 2101045.
7 X. Zhang, S. Wang, W. Zhu, Z. Cao, A. Wang and F. Hao, *Adv. Funct. Mater.*, 2022, **32**, 2108832.
8 J. Dong, S. Shao, S. Kahmann, A. Rommens, D. Hermida-Merino, G. Brink, M. Loi and G. Portale, *Adv. Funct. Mater.*, 2020, **30**, 2001294.
9 G. Nasti, M. Aldamasy, M. Flatken, P. Musto, P. Matczak, A. Dallmann, A. Hoell, A. Musiienko, H. Hempel and E. Aktas, *ACS Energy Lett.*, 2022, **7**, 3197–3203.
10 J. Qiu, Y. Lin, X. Ran, Q. Wei, X. Gao, Y. Xia, P. Müller-Buschbaum and Y. Chen, *Sci. China: Chem.*, 2021, **64**, 1577–1585.
11 S. Rühle, *J. Sol. Energy*, 2016, **130**, 139–147.
12 F. Zhang, Q. Zhang, X. Liu, Y. Hu, Z. Lou, Y. Hou and F. Teng, *ACS Appl. Mater. Interfaces*, 2021, **13**, 24272–24284.
13 C. Kuan, J. Chih, Y. Chen, B. Liu, C. Wang, C. Hou, J. Shyue and E. Diau, *ACS Energy Lett.*, 2022, **7**, 4436–4442.
14 H. Jia, H. Shi, R. Yu, H. Ma, Z. Wang, C. Zou and Z. Tan, *Small*, 2022, **18**, 2200036.
15 G. Li, Z. Su, M. Li, F. Yang, M. H. Aldamasy, J. Pascual, F. Yang, H. Liu, W. Zuo, D. Di Girolamo, Z. Iqbal, G. Nasti, A. Dallmann, X. Gao, Z. Wang, M. Saliba and A. Abate, *Adv. Energy Mater.*, 2021, 11.
16 X. Jiang, H. Li, Q. Zhou, Q. Wei, M. Wei, L. Jiang, Z. Wang, Z. Peng, F. Wang, Z. Zang, K. Xu, Y. Hou, S. Teale, W. Zhou, R. Si, X. Gao, E. Sargent and Z. Ning, *J. Am. Chem. Soc.*, 2021, **143**, 10970–10976.
17 M. Li, W. Zuo, Y. Yang, M. Aldamasy, Q. Wang, S. Cruz, S. Feng, M. Saliba, Z. Wang and A. Abate, *ACS Energy Lett.*, 2020, **5**, 1923–1929.
18 H. Li, Y. Xu, S. Ramakrishnan, Y. Zhang, M. Cotlet, T. Xu and Q. Yu, *Cell Rep. Phys. Sci.*, 2022, **3**, 101060.
19 K. Yan, M. Long, T. Zhang, Z. Wei, H. Chen, S. Yang and J. Xu, *J. Am. Chem. Soc.*, 2015, **137**, 4460–4468.
20 J. Kim, B.-w. Park, J. Baek, J. Yun, H. Kwon, J. Seidel, H. Min, S. Coelho, S. Lim and S. Huang, *J. Am. Chem. Soc.*, 2020, **142**, 6251–6260.
21 T. Zhang, T. Nakajima, H. Cao, Q. Sun, H. Ban, H. Pan, H. Yu, Z. Zhang, X. Zhang, Y. Shen and M. Wang, *ACS Appl. Mater. Interfaces*, 2021, **13**, 49907–49915.
22 T. Zhang, H. Ban, Q. Sun, H. Pan, H. Yu, Z. Zhang, X. Zhang, Y. Shen and M. Wang, *J. Energy Chem.*, 2022, **65**, 179–185.
23 X. Meng, Y. Li, Y. Qu, H. Chen, N. Jiang, M. Li, D. J. Xue, J. Hu, H. Huang and S. Yang, *Angew. Chem., Int. Ed.*, 2021, **133**, 3737–3742.
24 R. Schwartz, T. Schneller and R. Waser, *C. R. Chim.*, 2004, **7**, 433–461.
25 J. Lagerwall, C. Schütz, M. Salajkova, J. Noh, J. Hyun Park, G. Scalia and L. Bergström, *NPG Asia Mater.*, 2014, **6**, e80.
26 R. Kerner, L. Zhao, Z. Xiao and B. Rand, *J. Mater. Chem. A*, 2016, **4**, 8308–8315.
27 H. Gao, X. Meng, Y. Du and X. Gao, *Thin Solid Films*, 2019, **682**, 37–43.
28 J. Liu, X. Zheng, O. Mohammed and O. Bakr, *Acc. Chem. Res.*, 2022, **55**, 262–274.
29 A. Jana, A. Meena, S. Patil, Y. Jo, S. Cho, Y. Park, V. Sree, H. Kim, H. Im and R. Taylor, *Prog. Mater. Sci.*, 2022, 100975.
30 D. Geldart, *Powder Technol.*, 1972, **6**, 201–215.
31 D. Li, M. B. Müller, S. Gilje, R. B. Kaner and G. Wallace, *Nat. Nanotechnol.*, 2008, **3**, 101–105.
32 K. Chen and M. Elimelech, *Langmuir*, 2006, **22**, 10994–11001.
33 Y. Wang, W. Zhang, J. Shang, C. Shen and S. Joseph, *Environ. Sci. Technol.*, 2019, **53**, 8136–8146.
34 W. Yang, J. Shang, P. Sharma, B. Li, K. Liu and M. Flury, *Sci. Total Environ.*, 2019, **658**, 1306–1315.
35 W. Schmickler, *J. Solid State Electrochem.*, 2020, **24**, 2175–2176.
36 H. Ren, S. Yu, L. Chao, Y. Xia, Y. Sun, S. Zuo, F. Li, T. Niu, Y. Yang, H. Ju, B. Li, H. Du, X. Gao, J. Zhang, J. Wang, L. Zhang, Y. Chen and W. Huang, *Nat. Photonics*, 2020, **14**, 154–163.
37 J. Qiu, Y. Xia, Y. Zheng, W. Hui, H. Gu, W. Yuan, H. Yu, L. Chao, T. Niu, Y. Yang, X. Gao, Y. Chen and W. Huang, *ACS Energy Lett.*, 2019, **4**, 1513–1520.
38 P. Chen, Y. Bai, S. Wang, M. Lyu, J. H. Yun and L. Wang, *Adv. Funct. Mater.*, 2018, **28**, 1706923.
39 H. Ban, Q. Sun, T. Zhang, H. Li, Y. Shen and M. Wang, *Sol. RRL*, 2020, **4**, 1900457.

40 G. Xing, M. Kumar, W. Chong, X. Liu, Y. Cai, H. Ding, M. Asta, M. Grätzel, S. Mhaisalkar, N. Mathews and T. Sum, *Adv. Mater.*, 2016, **28**, 8191–8196.
41 H. Li, X. Wang, T. Zhang, X. Gong, Q. Sun, H. Pan, Y. Shen, S. Ahmad and M. Wang, *Adv. Funct. Mater.*, 2019, **29**, 1903293.
42 C. Ma, D. Shen, T. Ng, M. Lo and C. Lee, *Adv. Mater.*, 2018, **30**, 1800710.
43 H. Lai, B. Kan, T. Liu, N. Zheng, Z. Xie, T. Zhou, X. Wan, X. Zhang, Y. Liu and Y. Chen, *J. Am. Chem. Soc.*, 2018, **140**, 11639–11646.
44 C. Ni, Y. Huang, T. Zeng, D. Chen, H. Chen, M. Wei, A. Johnston, A. Proppe, Z. Ning, E. Sargent, P. Hu and Z. Yang, *Angew. Chem.*, 2020, **132**, 14081–14087.
45 H. Ban, T. Nakajima, Z. Liu, H. Yu, Q. Sun, L. Dai, Y. Shen, X. Zhang, J. Zhu, P. Chene and M. Wang, *J. Mater. Chem. A*, 2022, **10**, 3642–3649.
46 R. Yu, G. Wu, R. Shi, Z. Ma, Q. Dang, Y. Qing, C. Zhang, K. Xu and Z. Tan, *Adv. Energy Mater.*, 2023, **13**, 2203127.
47 X. Meng, J. Lin, X. Liu, X. He, Y. Wang, T. Noda, T. Wu, X. Yang and L. Han, *Adv. Mater.*, 2019, **31**, 1903721.
48 H. Pan, X. Zhao, X. Gong, H. Li, N. H. Ladi, X. L. Zhang, W. Huang, S. Ahmad, L. Ding, Y. Shen, M. Wang and Y. Fu, *Mater. Horiz.*, 2020, **7**, 2276–2291.
49 W. Zhang, Y. Xie, D. Xiong, X. Zeng, Z. Li, M. Wang, Y.-B. Cheng, W. Chen, K. Yan and S. Yang, *ACS Appl. Mater. Interfaces*, 2014, **6**, 9698–9704.
50 X. Gong, Q. Sun, S. Liu, P. Liao, Y. Shen, C. Grätzel, S. M. Zakeeruddin, M. Grätzel and M. Wang, *Nano Lett.*, 2018, **18**, 3969–3977.